GEOPHYSICS, VOL. 82, NO. 5 (SEPTEMBER-OCTOBER 2017); P. V285–V296, 14 FIGS.
10.1190/GEO2016-0116.1

A low-frequency deghosting method: Analysis and numerical tests

Ying Wang[1], Adriana Citlali Ramirez[2], and Are Osen[1]

ABSTRACT

The low-frequency component of seismic data can be beneficial for several reasons: improved signal penetration into the earth, enhanced resolution, and better constrained inversion results. We have developed a detailed analysis of a deghosting solution for the low-frequency spectrum of marine seismic pressure data. The advantages of this low-frequency deghosting method are: (1) it can be applied in the spatial domain, (2) it is applicable for horizontal streamers and for streamers with a mild depth variation, and (3) it is a fast-track solution that can be used flexibly as a preprocessing, or premigration step. The disadvantages of this method are: (1) it is an approximation to the full-deghosting operator and cannot infill the ghost notches of the spectrum, except near 0 Hz, and (2) it has decreasing effectiveness with a larger source/receiver depth. Numerical tests on the synthetic and field data sets indicate that this method is promising in deghosting data, up to at least half the frequency of the first nonzero ghost notch.

INTRODUCTION

The importance of broadening the bandwidth of seismic data has been increasingly evident for high-resolution imaging and inversion (impedance inversion and waveform inversion). This has created a search for new and improved acquisition techniques, as well as advanced methods for processing and imaging.

Among the methodologies for obtaining broader bandwidth in towed streamer data, deghosting or up/down separation has received a renewed interest in recent years. In marine seismic exploration, the presence of the sea surface generates two-way wavefield propagation by reflecting back (almost perfectly) all the energy that reaches this interface. The portion of the wavefield that interacts with the sea surface is referred to as ghost events. The ghost events are either (1) an upgoing wavefield propagated from the source, reflected at the sea surface, and further propagated down into the earth subsurface, or (2) a scattered wavefield (after interacting with the earth subsurface), reflected at the sea surface, and recorded as downgoing waves at the receivers. Ideally, up/down separation would allow selecting only the events starting their propagation as downgoing waves at the source and recorded at the receivers as upgoing waves, events that are ghost-free. The ghosting process causes a series of distinct notches in the frequency spectrum, and therefore reduces the useful bandwidth of the measured wavefield.

The ghosted pressure wavefield (e.g., measured towed streamer data) always has a notch at 0 Hz. We will refer to all other ghost notches as nonzero frequency ghost notches. The locations of the ghost notches are periodic along the frequency axis, and the period decreases as the streamer and/or the source is towed deeper. Consider a single primary and a single ghost associated with it, for vertical incidence, the first nonzero ghost notch in the amplitude spectrum is then found at the frequency equal to the ratio of water velocity and double the streamer depth. For example, a streamer towed at 5 m depth causes the first nonzero receiver ghost notch to appear at 150 Hz, whereas a streamer depth of 10 m provides a receiver ghost notch at 75 Hz.

The conventional practice is to tow the streamers close to the sea surface, such that the first nonzero ghost notch occurs beyond the maximum frequency of interest. However, shallow tow (e.g., 5 m) has a more detrimental effect on the low frequencies compared with a deep tow (e.g., 20 m). Besides, the signal-to-noise ratio (S/N) tends to be lower when the streamers are towed closer to the sea surface (Tabti et al., 2009). Thus, a deeper towing depth is considered advantageous.

There are many new seismic acquisition technologies aiming at acquiring data for improved deghosting. These new technologies include dual-component and multicomponent streamers (Carlson, 2007; van Manen et al., 2012; Mellier et al., 2014). Directional information can be included in data acquired with these new types of hardware and the recorded wavefield can therefore be decomposed

Manuscript received by the Editor 4 March 2016; revised manuscript received 7 April 2017; published ahead of production 15 May 2017; published online 27 June 2017.
[1]Formerly Statoil, Beijing, China. E-mail: sommeren@sina.com; Are.Osen@akerbp.com.
[2]Statoil, Beijing, China. E-mail: adper@statoil.com.

into upgoing and downgoing wavefields. The data are ghost-free if the decomposed data contain only the downgoing component at each source and the upgoing component at receivers. New processing schemes are required to deal with such new types of data. Klüver and Day (2011) propose a method to decompose 3D dual-sensor streamer data into upgoing/downgoing wavefield using crossline slowness estimates. Robertsson et al. (2008) discuss how multicomponent (three wavefield components) measurements could be used for 3D deghosting and for reconstructing/interpolating deghosted data between streamers. Özbek et al. (2010) show how the generalized matching pursuit algorithm could be used on such multicomponent data to reconstruct upgoing and downgoing pressure wavefields on a densely sampled grid. Andersson et al. (2016) present a 3D method for interpolation and deghosting based on structure tensors that do not have any assumptions about the water column or the sea surface.

There are also pure processing methods to deal with single-component measurements, i.e., conventional horizontal streamer data and slanted or variable-depth streamer data. Most of these single-component deghosting methods are based on wave theory and/or use signal-processing techniques. For example, there are Green's theorem-driven methods that have been well-described and demonstrated in a series of papers, e.g., Weglein et al. (2002), Zhang and Weglein (2005), Yarman and Ramirez (2013), and Mayhan and Weglein (2013). In a recently published paper by Amundsen et al. (2016), the authors provided a generalized method that simplifies the previous deghosting theories based on Green's theorem. There are also filter-based methods, in which the inverse of the ghost function would be applied on the pressure recordings as a deghosting filter. The deghosting filter is commonly represented in the frequency-wavenumber $(\omega\text{-}k_x\text{-}k_y)$ domain or, alternatively in its equivalent, the intercept time-slowness $(\tau\text{-}p_x\text{-}p_y)$ domain. Such methods are sensitive to the S/N, but they can often provide effective deghosting under certain controlled conditions, such as assumptions about the sea surface and the properties of the water column (Masoomzadeh and Woodburn, 2013; Wang et al., 2016). There are also various schemes aiming at deghosting for variable-depth streamer data being developed in recent years (Soubaras, 2012; Poole, 2013; Robertsson and Amundsen, 2014; Grion et al., 2016). The available frequency bandwidth can be increased considerably with the diversity of receiver ghosts being introduced by the variable depth profile of the receivers, in combination with corresponding deghosting methods to deal with such data.

It is well-known that low frequencies are important (Ten Kroode et al., 2013): They suffer less from the attenuation in the earth and can therefore penetrate deeper. They are also beneficial for waveform and impedance inversion because the inversion algorithms need low-frequency information to work and/or to be better constrained. There are situations in seismic processing in which we are only interested in migrating and using relatively low frequencies (up to approximately 30 Hz), such as RTM in some deep-water scenarios, or fast tracks. In this paper, we study a fast filter-based deghosting method that aims at improving low frequencies by filling in the first ghost notch around 0 Hz. The concept was originally proposed by Amundsen and Zhou (2013) and later studied by Wang et al. (2013). Basically, the method suggests a Taylor series expansion of the exact deghosting filter, which can be applied on seismic data in the frequency-space domain. Considering practical issues in terms of numerical implementation, we study the first two terms in the series expansion, which form the low-frequency approximation to the exact deghosting filter. The approximation removes the ghost effect within a certain range that will be discussed in the later sections. The method can be applied trace-by-trace sequentially to shot records using only a few neighboring traces at each trace entry, which gives it the flexibility to work for horizontal steamers as well as streamers with a mild depth variation. Similarly, when being used for source deghosting, the method should be applied to common-receiver gathers.

We will present an analysis of the effectiveness of this approximation, give numerical tests and initial application results on field data in the following sections.

THEORY

Assume that the reflection coefficient r_0 at the flat sea surface is constant (close to -1), then the ghost function for 3D propagation in the frequency-wavenumber domain (Amundsen, 1993) is

$$G(\omega, k_x, k_y) = 1 + r_0 e^{2ik_z z}, \tag{1}$$

with vertical wavenumber $k_z = \sqrt{k^2 - k_x^2 - k_y^2}$, where $k = \omega/c$ is the magnitude of the wavenumber, $\omega = 2\pi f$ is the angular frequency, c is the water velocity, k_x and k_y are the horizontal wavenumbers being Fourier conjugate variables for x and y, respectively. In the following discussion, the direction x is considered to be inline to the source direction in a given sail line and y is the crossline direction. The depth variable z is chosen to represent either the source depth z_s or the receiver depth z_r.

The ghost effects are angle dependent. The interference between the ghost-free data and the ghosts, e.g., receiver ghosts, creates notches in the amplitude spectrum of the recorded data at frequencies

$$f_n^r = \frac{nc}{2z_r \cos \alpha_r}, \quad n = 0, 1, 2, \ldots, \tag{2}$$

where α_r is the incidence angle of the wavefield recorded at the receiver. The source-side ghost notches appear at frequencies given by

$$f_n^s = \frac{nc}{2z_s \cos \alpha_s}, \quad n = 0, 1, 2, \ldots, \tag{3}$$

where α_s is the take-off angle at the source.

The 3D ghost effects can be eliminated theoretically in the frequency-wavenumber domain by applying a deghosting filter F to the given input pressure data p; i.e.,

$$p^{\mathrm{DG}}(\omega, k_x, k_y) = F(\omega, k_x, k_y) p(\omega, k_x, k_y), \tag{4}$$

where p^{DG} is the deghosted data and the filter F is the inverse of the ghost function expressed in equation 1. However, when it comes to implementation, the direct application of this 3D scheme requires us to apply 3D Fourier transforms to the pressure data with respect to time t and inline and crossline directions x and y, respectively. For towed-streamer data sets, the crossline wavenumber axis is usually heavily aliased due to sparse sampling. Because of this, a common practice is to assume $k_y = 0$ in the deghosting filter and use the 2D version of the deghosting scheme:

$$p^{\mathrm{DG}}(\omega, k_x) = F(\omega, k_x)p(\omega, k_x). \quad (5)$$

We call the filter F in equation 5 the 2D exact deghosting operator, and it has the following full expression:

$$F(\omega, k_x) = \frac{1}{1 + r_0 e^{2iz\sqrt{k^2 - k_x^2}}}. \quad (6)$$

By a variable change $u = k_x^2$, $F(\omega, k_x)$ can be written as a function of u:

$$F(u) = \frac{1}{1 + r_0 e^{2iz\sqrt{k^2 - u}}}. \quad (7)$$

A Taylor series expansion of $F(u)$ at $u = 0$ is described as Maclaurin's series:

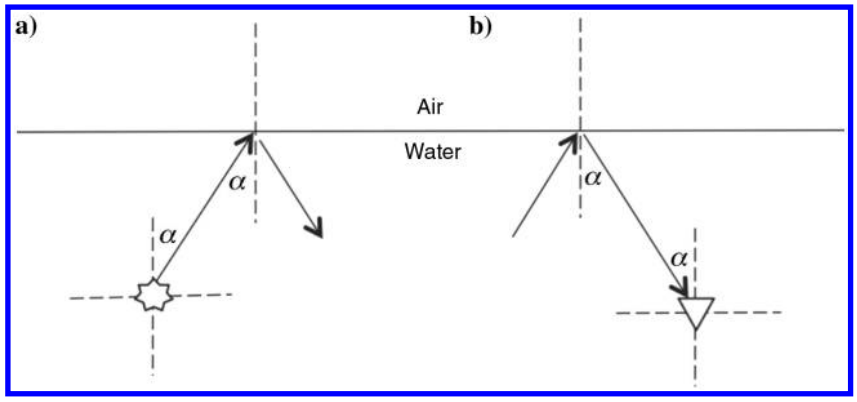

Figure 1. Reflection angle α at the sea surface. (a) For source-side ghosts, α is the take-off angle of the wavefield from the source, upgoing to the sea surface. (b) For receiver-side ghosts, α is the incident angle of the wavefield reflected by the sea surface, downgoing to the receiver locations.

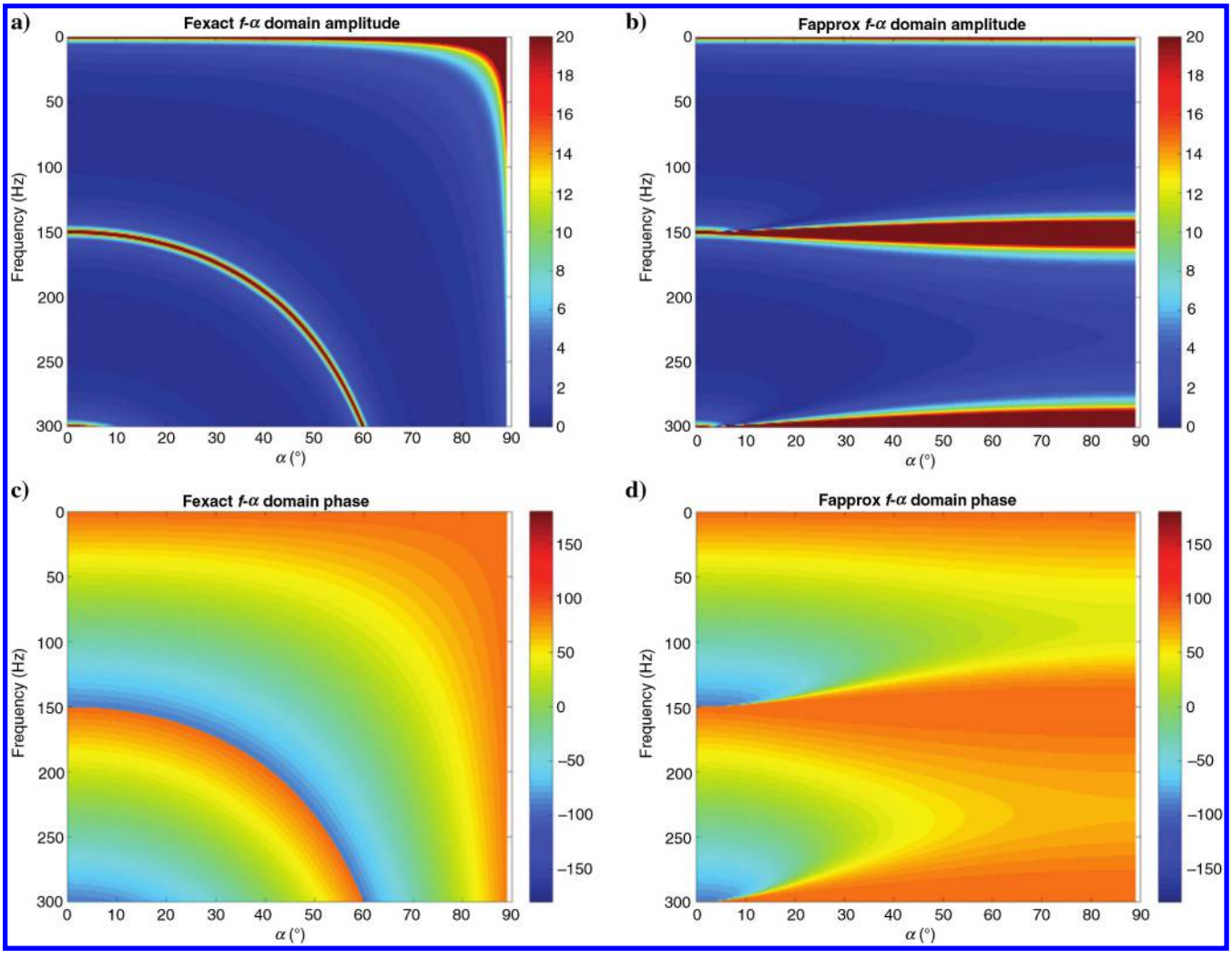

Figure 2. Amplitude and phase response with respect to frequency f and reflection angle α for the case in which $z = 5$ m. (a and b) The amplitude spectra of F_{exact} and F_{approx}, respectively. The color scale gives the amplitude value ranging from small (dark blue) to large (dark red). (c and d) The phase spectra of F_{exact} and F_{approx}, respectively. The color scale gives the phase angle value ranging from $-180°$ (dark blue) to $+180°$ (dark red).

$$F(u) = F(0) + uF'(0) + \frac{u^2}{2!}F''(0) + \ldots + \frac{u^n}{n!}F^{(n)}(0) + \ldots. \quad (8)$$

For practical reasons, we limit the expansion to the first order and truncate all higher order terms. The resulting approximation in terms of the original variable k_x^2 reads

$$F(\omega, k_x) \approx F(0) + F'(0)k_x^2, \quad (9)$$

where

$$F(0) = \frac{1}{G(k,z)}, \qquad F'(0) = \frac{izr_0 e^{2ikz}}{kG(k,z)^2}. \quad (10)$$

Here, $F(0)$ is the 1D normal incidence deghosting operator with $G(k,z) = 1 + r_0 e^{2ikz}$ being the ghost function when $k_x = k_y = 0$. The term $F'(0)k_x^2$ contributes to the inline aperture of the approximate deghosting filter (equation 9). By making use of the Fourier transform property based on $\partial_x^n e^{ik_x x} = (ik_x)^n e^{ik_x x}$, the following relationship stands:

$$\partial_x^2 p(\omega, x) \leftrightarrow (ik_x)^2 p(\omega, k_x) = -k_x^2 p(\omega, k_x), \quad (11)$$

where $p(\omega, x)$ is the frequency-space domain representation of the recorded pressure data, and $p(\omega, k_x)$ is the frequency-wavenumber domain representation, which is obtained by performing a Fourier transform to $p(\omega, x)$ in the inline direction. Notice that $F(0)$ and $F'(0)$ do not depend on k_x, but only on k, which can be calculated from ω/c. This fact, together with equation 11, implies that our approximate deghosting operator 9 can be carried out in the frequency-space domain. Insertion of equation 9 into the 2D deghosting scheme given in equation 5, and using the relationship in equation 11, we then have deduced the 2D frequency-space domain approximate deghosting formulation:

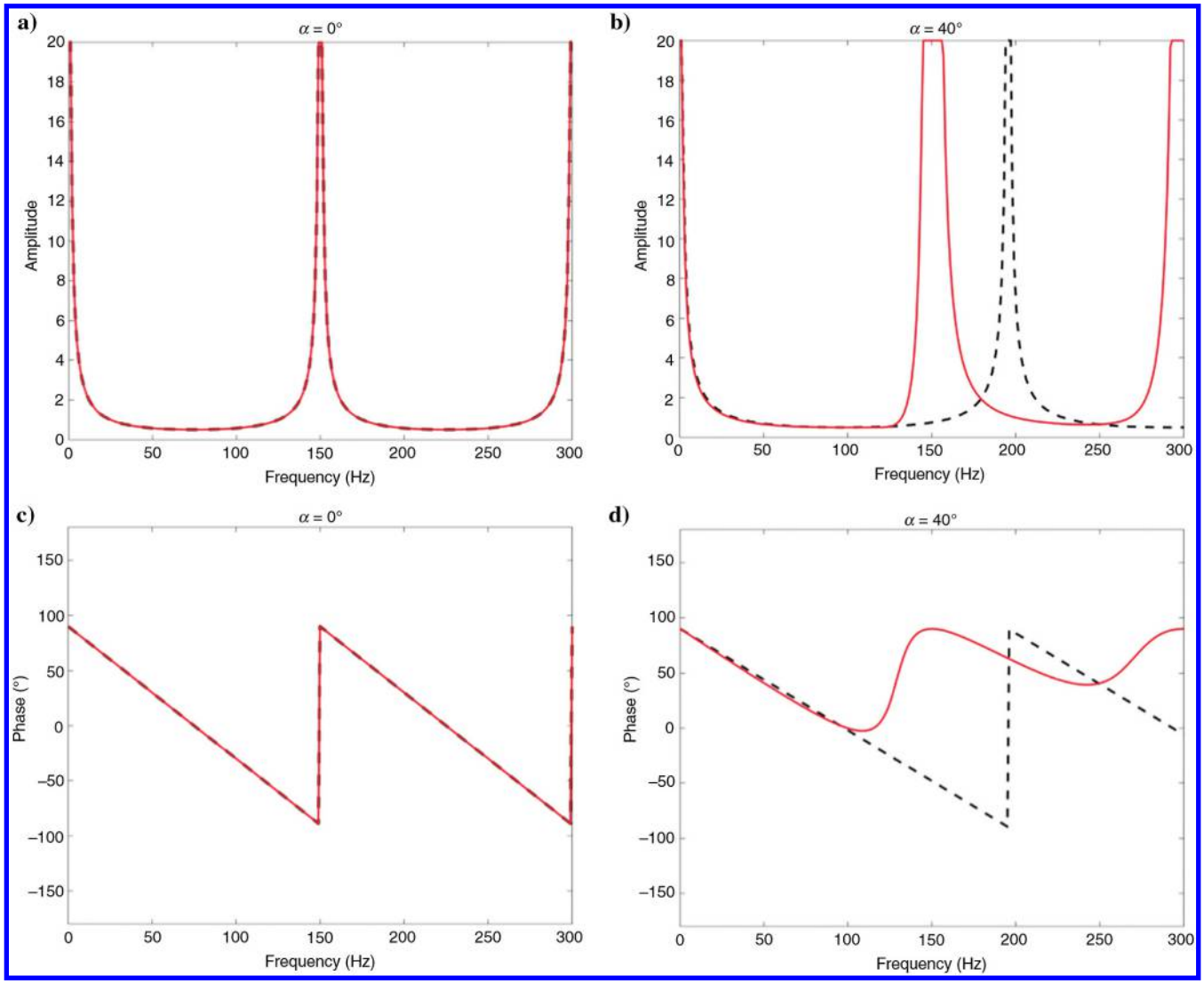

Figure 3. Detailed comparisons between F_{exact} (dashed black lines) and F_{approx} (solid red lines), when $z = 5$ m. (a and b) The amplitude spectra comparisons at $\alpha = 0°$ and at $\alpha = 40°$, respectively. (c and d) The phase comparisons at $\alpha = 0°$ and at $\alpha = 40°$, respectively.

$$p^{\mathrm{DG}}(\omega, x) \approx F(0)p(\omega, x) - F'(0)\partial_x^2 p(\omega, x). \quad (12)$$

The coefficients $F(0)$ and $F'(0)$ take into account the receivers (or sources) depth variation z and are functions of ω, c, and z. They are independent of the horizontal Cartesian coordinates, whereas the spatial partial derivative $\partial_x^2 p(\omega, x)$ involves the inline positions of the receivers (or sources) and can be approximated by finite differences (e.g., the three-point central difference operator). One attractive feature of this method is that the deghosting filter is local: The implementation of equation 12 only requires a 1D Fourier transform to the recorded pressure field along the time axis trace-by-trace; to approximately deghost the pressure field at a particular receiver (or source) location, only the pressure field at this and the two (or more, depending on the finite-difference scheme chosen for calculating the spatial derivative term) neighboring receivers (or sources) are required.

In the following sections, we will present the analysis of the effectiveness of the approximate deghosting scheme deduced above, and the test results of its application on the synthetic and field data.

EFFECTIVENESS ANALYSIS

We propose to investigate the range of effectiveness of the approximate deghosting method in terms of the temporal frequency f and the reflection angle α, considering the angle dependency of the ghost effects.

In a 2D scenario, the following relationships between the spatial and temporal wavenumbers hold:

$$k_z = k\cos\alpha, \quad k_x = k\sin\alpha, \quad \text{s.t.} \quad k_z = \sqrt{k^2 - k_x^2}, \quad (13)$$

where α represents the reflection angle at the sea surface in x-z plane. To be more specific, if we consider the source-side ghost, α is the take-off angle of the wavefield from the source, upgoing to the sea surface; whereas for the receiver-side ghost, α is the incidence angle of the wavefield reflected by the sea surface, downgoing to the receiver locations (Figure 1). We denote F_{exact} as the f-α domain equivalence for the 2D exact deghosting operator 6 and F_{approx} for the approximate deghosting operator 9. Using the relationship in equation 13, they have the following expressions:

$$F_{\mathrm{exact}} = \frac{1}{1 + r_0 e^{2izk\cos\alpha}}, \quad (14)$$

$$F_{\mathrm{approx}} = F(0) + F'(0)(k\sin\alpha)^2, \quad (15)$$

where $k = \omega/c$ and $\omega = 2\pi f$, $F(0)$ and $F'(0)$ were given in equation 10 in terms of k.

Consider the case when the receivers (or sources) are towed at depth $z = 5$ m. By setting the water velocity $c = 1500$ m/s and the sea-surface reflection coefficient $r_0 = -1$, we compare the amplitude and phase spectra of the deghosting operators, F_{exact} and F_{approx}, in the f-α domain.

Figure 2a and 2b gives the amplitude spectra of F_{exact} and F_{approx}, respectively. In both figure parts, we use the same color bar showing the amplitude range from 0 (blue) to 20 (red). High-amplitude areas (dark red color) mark the positions of the ghost notches. For example, in Figure 2a, the angle-dependent notch positions are exactly as expressed in equation 2 (or equation 3); whereas in Figure 2b, F_{approx} predicts the positions of all the notches of F_{exact} for a small range near the zero-reflection angle (at around 0, 150, and 300 Hz); however, as the reflection angle gets larger, the predictions begin to deviate from the true notch positions given by F_{exact}. Phase spectra of both operators are given in Figure 2c and 2d. The color bar marks the phase angle ranging from $-180°$ (blue) to 180° (red). By visual inspection of these two figure parts we see that F_{approx} approximates F_{exact} for low frequencies (from 0 Hz till a little less than the first nonzero ghost notch 150 Hz) within a certain reflection angle range (from 0° to approximately 45°).

As a more detailed illustration, we plot the amplitude spectra of both deghosting filters together at two representative reflection angles in Figure 3a and 3b. Clearly, as shown in Figure 3a, when $\alpha = 0°$, F_{approx} (red solid line) has the perfect approximation to F_{exact} (dashed black line) at all frequencies. In Figure 3b, we give the comparison at a larger reflection angle, i.e., when $\alpha = 40°$. In this situation, F_{approx} gives a good approximation to F_{exact} at the low frequencies (from 0 to approximately 125 Hz), whereas it fails to predict the true position of the first nonzero ghost notch at approximately 200 Hz. Figure 3c and 3d shows the detailed phase-spectra comparisons at these two reflection angles, 0° and 40°, respectively. The observation of the approximation effects is consistent with that of the amplitude analysis shown in Figure 3a and 3b.

For the last part of the analysis, we study the relative difference between the two operators, i.e., $[\mathrm{abs}((F_{\mathrm{exact}} - F_{\mathrm{approx}})/F_{\mathrm{exact}})]$. Figure 4 shows the contours in the f-α domain when this value is less than 2%, 4%, 6%, and 8%, respectively; it also indicates that F_{approx} serves as a good approximation to F_{exact} in the blue area, where the relative difference is approximately less than 5%. The dark red color in this figure marks the area in which the difference is larger than 10%.

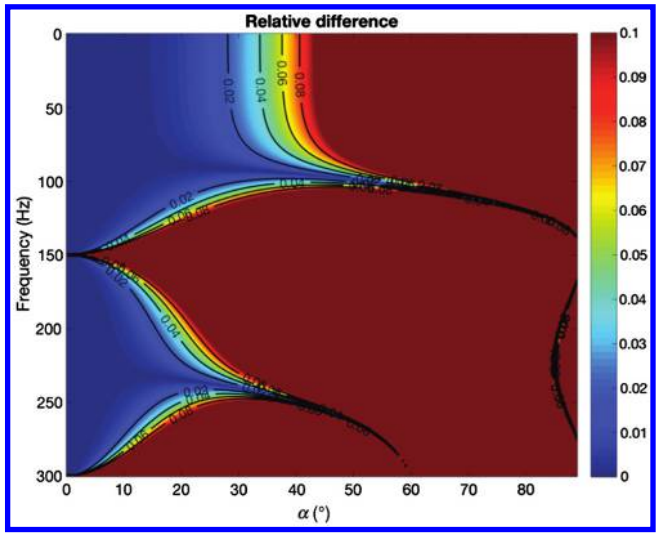

Figure 4. Relative difference between F_{approx} and F_{exact} for the case when $z = 5$ m. The black contour lines indicate the boundaries of the areas in which $\mathrm{abs}((F_{\mathrm{exact}} - F_{\mathrm{approx}})/(F_{\mathrm{exact}})) < 2\%$, 4%, 6%, and 8%, respectively.

The displays in Figures 2–4 are limited to the analysis of a single configuration, when $z = 5$ m. In this case, the effective range of F_{approx}, i.e., the blue area in Figure 4, is approximately from 0° to 40° for frequencies up to approximately 100 Hz. We also tested cases when $z = 10, 15, 20$ m, ... For example, in Figures 5, 6, and 7, we present the analysis being done for the case when $z = 10$ m. From those sets of tests, we conclude that the towing depth does not affect the relative range of effectiveness in terms of the frequency, which is from 0 Hz to at least half of the first nonzero ghost notch frequency. This means a decrease of the absolute effective frequency range as the towing depth increases. If we look at the range of effectiveness in terms of the reflection angle, F_{approx} can stably attenuate the ghost effects to at least 40, and this range is the same for different towing depths.

Before showing test results on synthetic and real data of this low-frequency deghosting scheme under discussion, we need to clarify the following: (1) The frequency-reflection angle domain expression 15 is what we used for intuitive analysis of the effective range of the method, and it is not directly applicable to the data; (2) application of the frequency-wavenumber domain expression 9 is not ideal because it requires a spatial Fourier transform of data in the inline direction, which has problems when the depth profile of the receivers or (sources) is not horizontal; (3) the frequency-space domain implementation expressed by equation 12 is the one to be applied on seismic pressure data. It is a semilocal operator that can be applied in short spatial windows — at each trace location, operator 12 needs only a few nearby traces to calculate the derivatives in the inline direction. In recent years, common streamer configurations for slanted streamers (flat or curved) have a gradient (the difference between the frontmost receiver and the last-used receiver) of 10–30 m. Considering streamer lengths of 6–10 km, the variation within neighboring receivers is in the order of centimeters. Thus, the finite-difference calculation of the derivatives is an acceptable approximation for variable depth cables when the curvatures are mild. Therefore, in all examples below, we perform the low-frequency deghosting tests with equation 12.

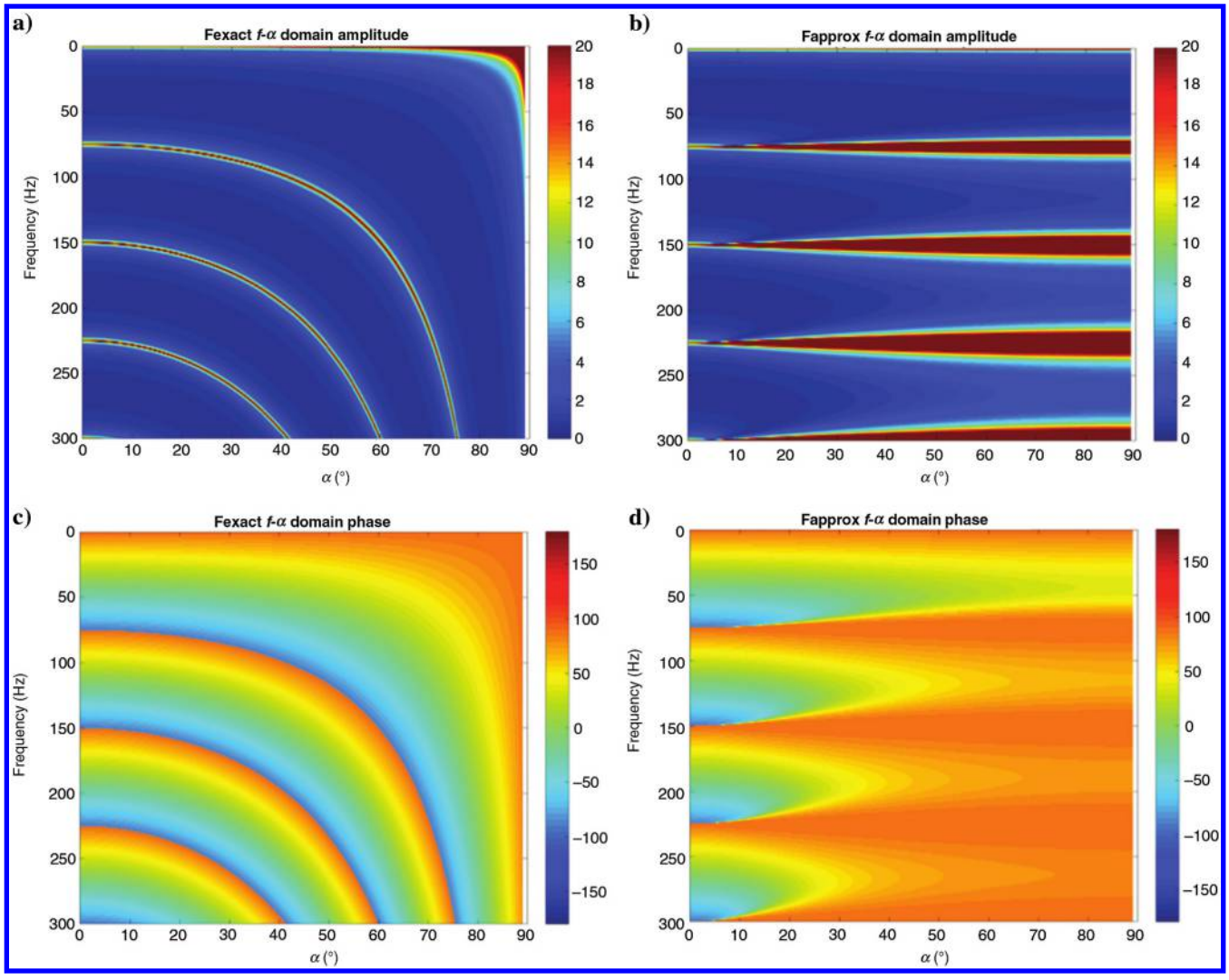

Figure 5. Amplitude and phase response with respect to frequency f and reflection angle α for the case when $z = 10$ m. (a and b) The amplitude spectra of F_{exact} and F_{approx}, respectively. (c and d) The phase spectra of F_{exact} and F_{approx}, respectively.

EXAMPLES

Synthetic data example

We have modeled one gather of data with a simplified scenario, and the modeling configuration is illustrated in Figure 8. The data are modeled for a streamer with receiver depths z_r, varying in the range of 3–12 m to simulate a mildly slanted streamer acquisition. The receiver spacing along the streamer is 3 m. We use a velocity model consisting of a half-space of water and a reflecting boundary above it to mimic the air-water contact; all other sides of the model are absorbing boundaries. We model with analytic Green's functions by putting a source (the "imaginary source" as marked in Figure 8) at a depth of 750 m below the air-water contact. This configuration equals to the situation, in which only downgoing waves (the dashed red and blue lines) have been produced by a source being placed close to the sea surface, and they are reflected at the imaginary reflector and go upward. No source ghost would be recorded in our case by putting the imaginary source deep. The red event (solid red line) is a primary that arrives as an upgoing wavefield at the receiver locations, whereas the blue event (solid blue

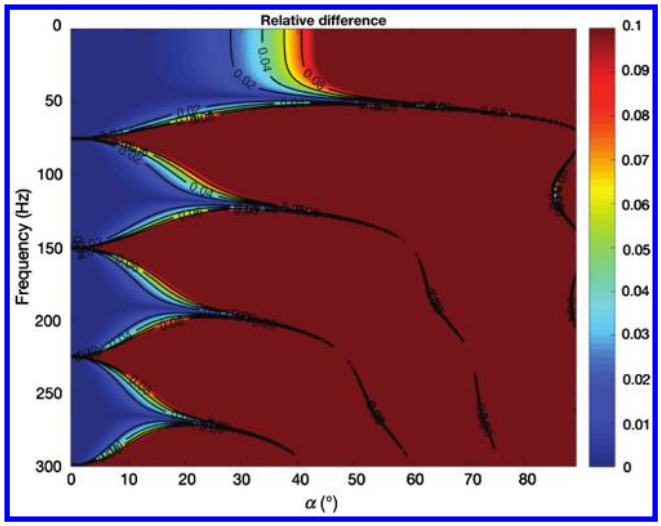

Figure 7. Relative difference between F_{approx} and F_{exact} for the case when $z = 10$ m. The black contour lines indicate the boundaries of the areas in which abs$((F_{exact} - F_{approx})/(F_{exact})) < 2\%$, 4%, 6%, and 8%, respectively.

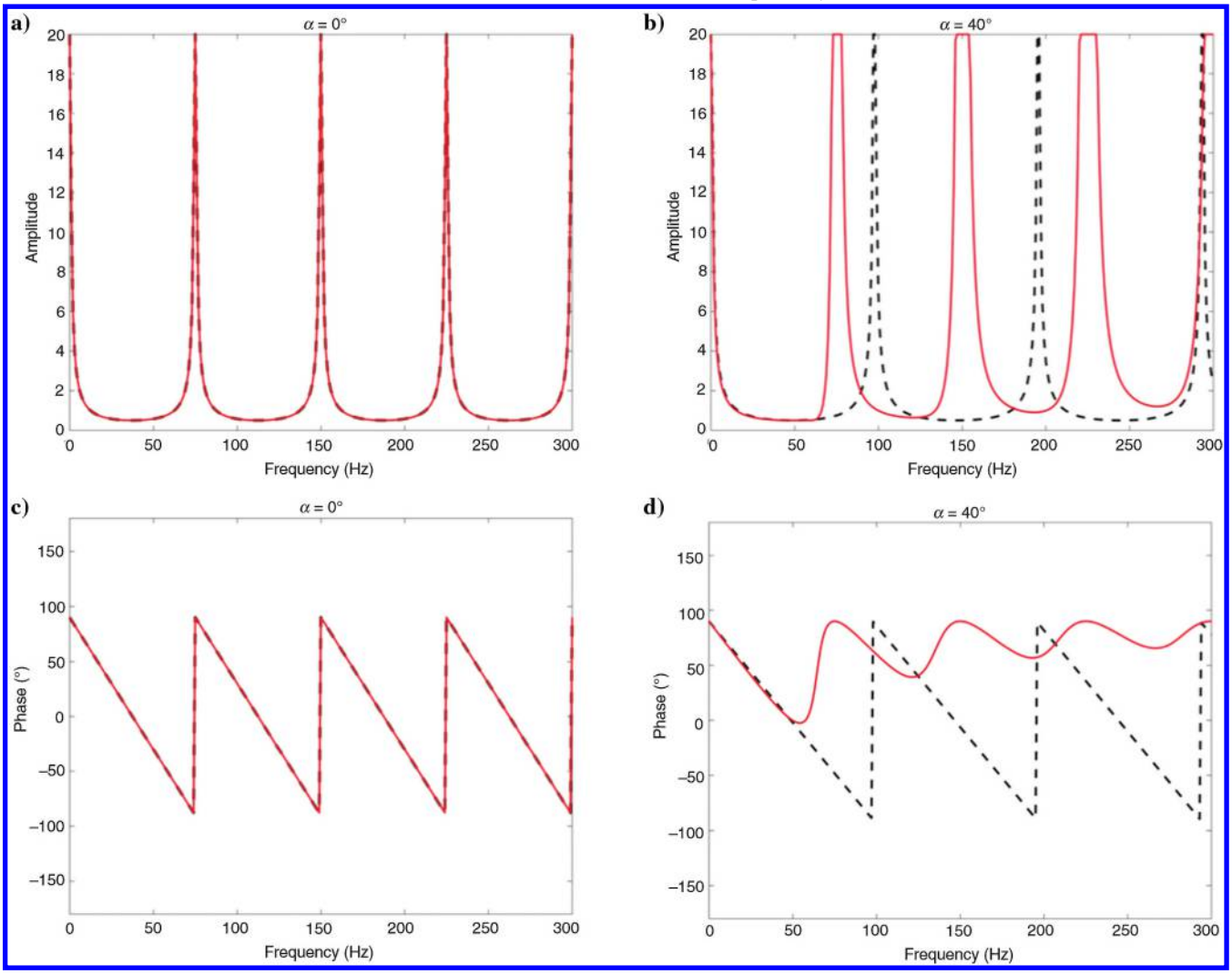

Figure 6. Detailed comparisons between F_{exact} (dashed black lines) and F_{approx} (solid red lines), when $z = 10$ m. (a and b) The amplitude spectra comparisons at $\alpha = 0°$ and at $\alpha = 40°$, respectively; (c and d) The phase comparisons at $\alpha = 0°$ and at $\alpha = 40°$, respectively.

line) is the downgoing receiver ghost. The upgoing and downgoing events are recorded at the receivers to form the ghosted data as input to our test. The largest offset in this example is 3000 m and the corresponding maximum incidence angle is approximately 75°. As a benchmark, we also have modeled the data without ghost effects by switching the reflecting boundary into an absorbing boundary at the air-water contact. We apply equation 12 as the deghosting operator to the data for all frequencies. Because the streamer depths are shallow, the first nonzero ghost notch should appear at a frequency larger than the maximum frequency of the modeled data. Thus, we cannot visually observe the first nonzero ghost notch in the amplitude spectrum of the ghosted data. We aim to use this example to demonstrate that for data with the maximum frequency below the first nonzero ghost notch, the low-frequency deghosting scheme works for gently sloping steamers.

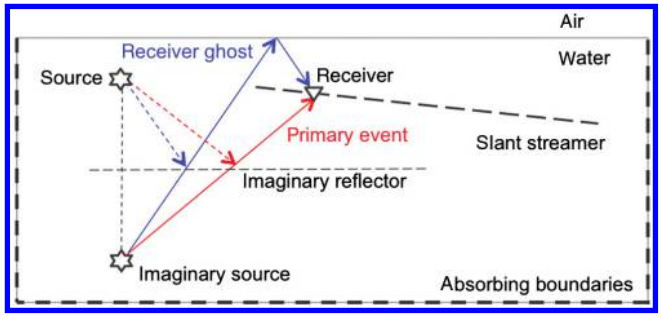

Figure 8. Illustration of the synthetic model configuration: shallow-tow slanted streamer data. An imaginary source is put deeper than the slanted streamer so that it produces a primary event and a receiver ghost associated with it; no source ghost is generated in this configuration

Figure 9a displays the waveforms of the input data containing the upgoing wave and its receiver ghost. Figure 9b shows the deghosted data, whereas Figure 9c shows the benchmark, i.e., the modeled upgoing wave only (without any ghost). Figure 9d–9f shows the amplitude spectra corresponding to Figure 9a–9c, respectively. Comparing Figure 9a–9c, we can see that the ghost event has been removed from all traces and the primary upgoing event has been recovered. A closer look at the waveform for the traces with larger offsets (larger incidence angles) shows that waveform recovery is not as good as the one at smaller offsets (e.g., compare the waveforms between trace numbers 600–1000, and the waveforms between trace numbers 0–400 in Figure 9b with the waveforms in Figure 9c). This is because we applied the method to all traces/all incidence angles (0°–75°), whereas our method gives a good approximation only up to approximately 40°. This result is therefore in accordance with our analysis. Comparing Figure 9d–9f, we can

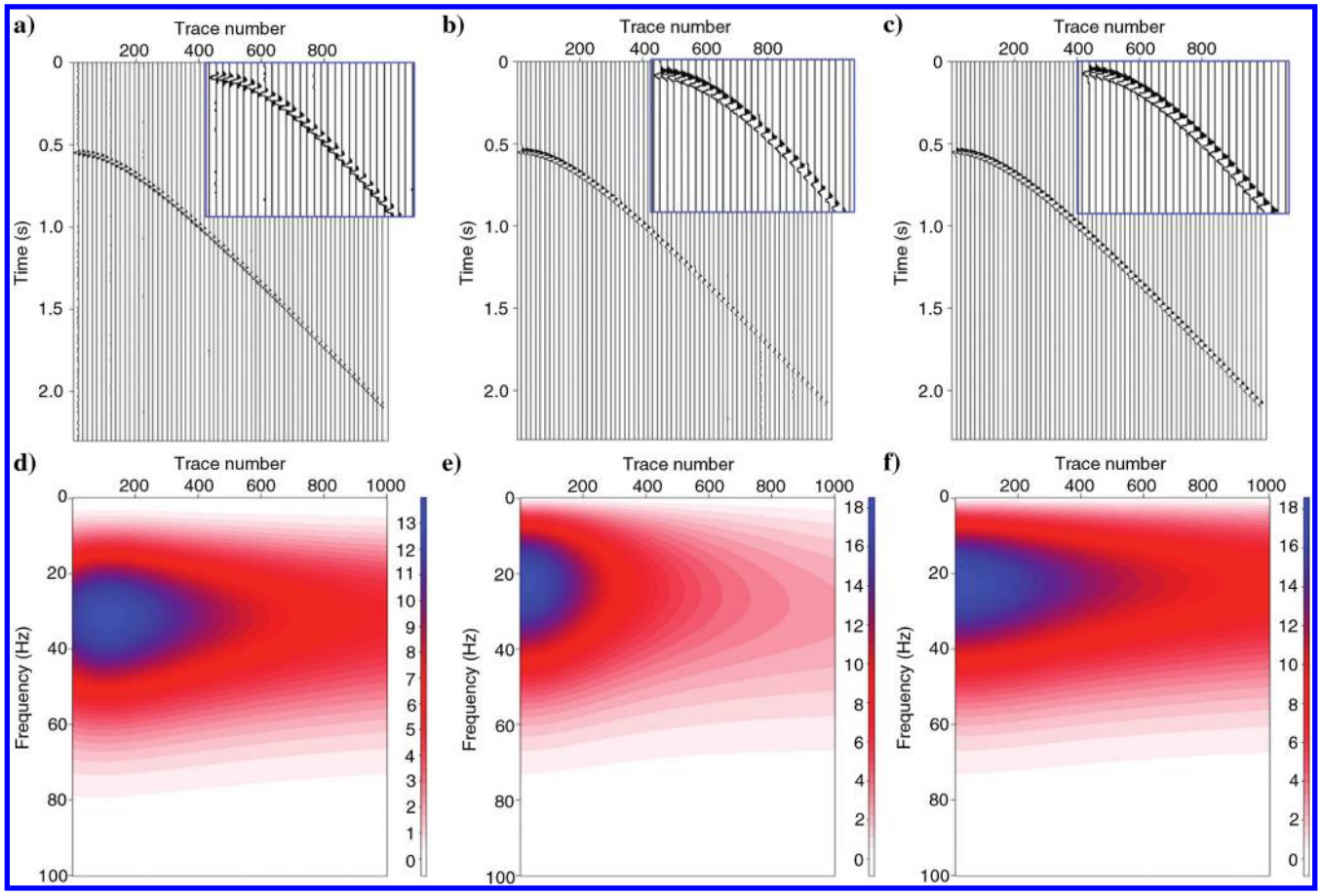

Figure 9. Shallow-tow slanted streamer synthetic example. Top row: Data. (a) Data with ghost, (b) deghosted data, and (c) benchmark. The blue boxes in (a-c) are the magnified waveforms of the first 400 traces. Bottom row: Amplitude spectra. Panels (d-f) correspond to (a-c), respectively. The blue areas (with large amplitude values) indicate the positions of the dominant frequency, respectively.

see that the low-frequency amplitudes are compensated and the dominant frequency has been corrected to the right place after deghosting. To be specific, in Figure 9d, the amplitude spectrum of the ghosted data shows that the dominant frequency is at approximately 32.5 Hz, whereas the low-frequency content at approximately 0 Hz is attenuated by the ghost effect; Figure 9e shows improved frequency content on the lower end and the dominant frequency is now at approximately 22.5 Hz after deghosting; Figure 9f displays the benchmark indicating the effectiveness of the low-frequency deghosting method.

Field data example — Application on Troll field data

We extracted a 2D sail-line from a 3D data set acquired over the Troll field in the North Sea, which contained 123 shots and 1 streamer with 190 receivers. The sources were towed at 4 m depth with 37.5 m intervals. The streamer was towed at a constant depth of 6 m with a nominal receiver interval of 12.5 m. According to the previous analysis on the effectiveness range of our method, we should apply the receiver-side low-frequency deghosting to the data within the frequency range between 0 Hz up to half of the first

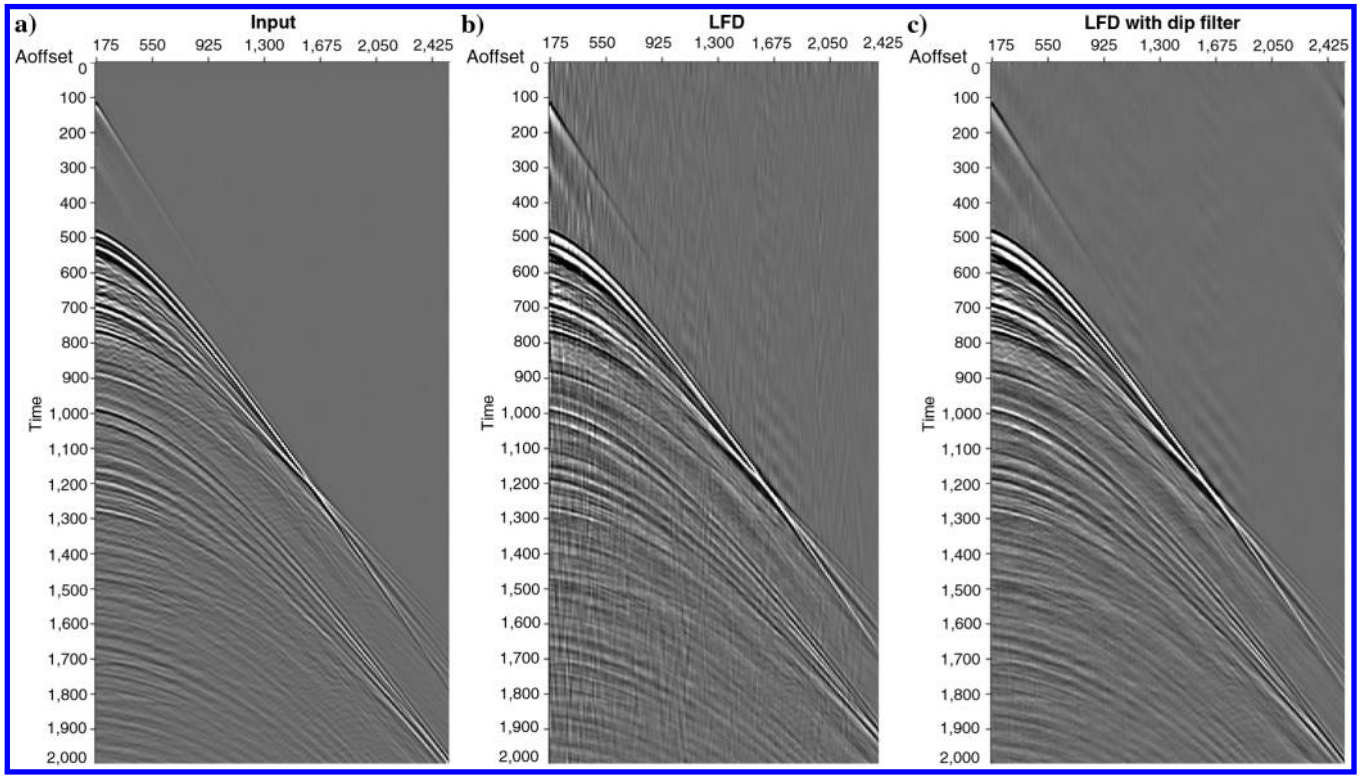

Figure 10. Field-data example from the Troll field. Comparison on one shot gather in t-x domain: (a) Input raw data, (b) after low-frequency deghosting on the receiver side, and (c) after applying a dip filter to the low-frequency deghosting result with the boosted low-frequency noise being removed.

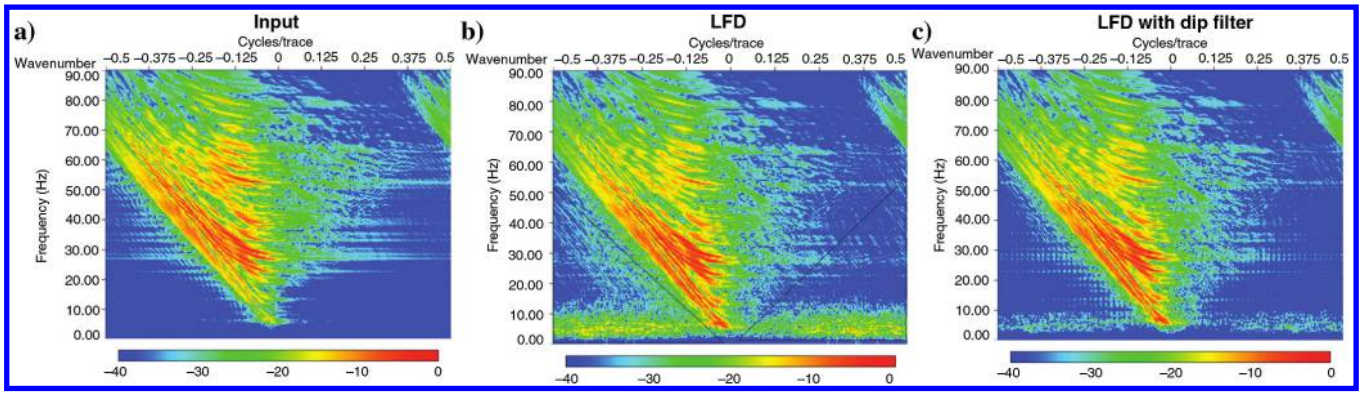

Figure 11. Field-data example from the Troll field. Comparison on one shot gather in f-k domain: (a) Input raw data, (b) after low-frequency deghosting on the receiver side — the black polygon marks the area with the boosted low-frequency noise — and (c) after applying a dip filter to the low-frequency deghosting with the boosted noise being removed.

nonzero receiver-side ghost notch frequency, which is approximately 62.5 Hz for zero offset. For this, a high-cut filter has been applied to the recorded data prior to deghosting, such that the input data have a bandwidth of approximately 65 Hz.

We first present the receiver-side low-frequency deghosting result of one shot gather in Figures 10–12. Note that in each of these figures, the same display mode (color scale, gain factor, etc.) has been used. Figures 10 and 11 give the comparisons in the t-x domain and in the f-k domain, respectively. Figures 10a and 11a show the input data, whereas Figures 10b and 11b show the deghosted data. The improved low-frequency content is visible in both domains as well as the boosted noise around 0 Hz. The boosted low-frequency noise is then observed to be mostly outside of the main signal cone in the f-k domain as shown in Figure 11b, indicated by the polygon with a black contour. A dip filter (f-k domain filter) has then been applied to remove the noise. Figures 10c and 11c show the dip-filtered low-frequency deghosting result. In Figure 12, we present the amplitude spectra comparison among these three sets of data. Notice the enhanced low frequencies after low-frequency deghosting (red) relative to the input data (black); then, after the application of the dip filter, some of the low-frequency noise has been removed (green).

The prestack time-migrated images are shown in Figure 13, in which the unghosted data (Figure 13a) and the receiver-side low-frequency deghosted plus dip-filtered data (Figure 13b) are compared. Notice the improved low-frequency content and the

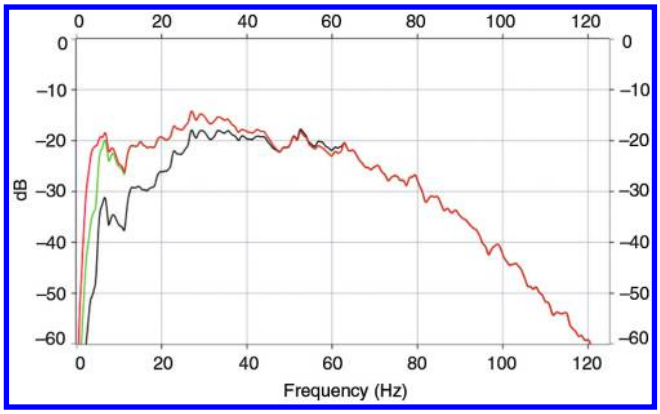

Figure 12. Field-data example from the Troll field. Comparison of amplitude spectra on one shot gather: Input raw data (black), after low-frequency deghosting on the receiver side (red), and after applying a dip filter to the low-frequency deghosting result with the boosted low-frequency noise being removed (green).

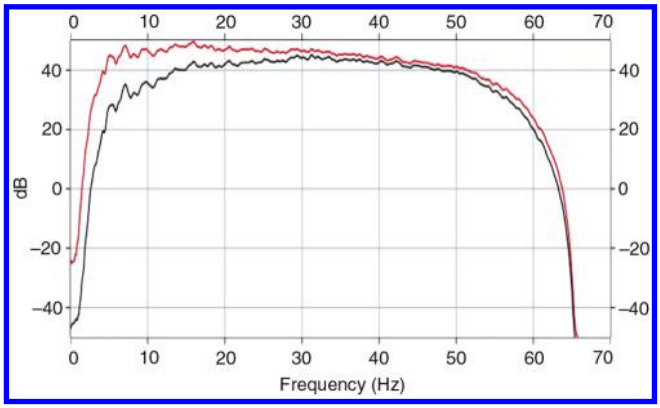

Figure 14. Field-data example from the Troll field, the premigration application. The amplitude spectra comparion on the prestack time-migrated panels before (black) and after (red) low-frequency deghosting on the receiver side (plus a dip filter).

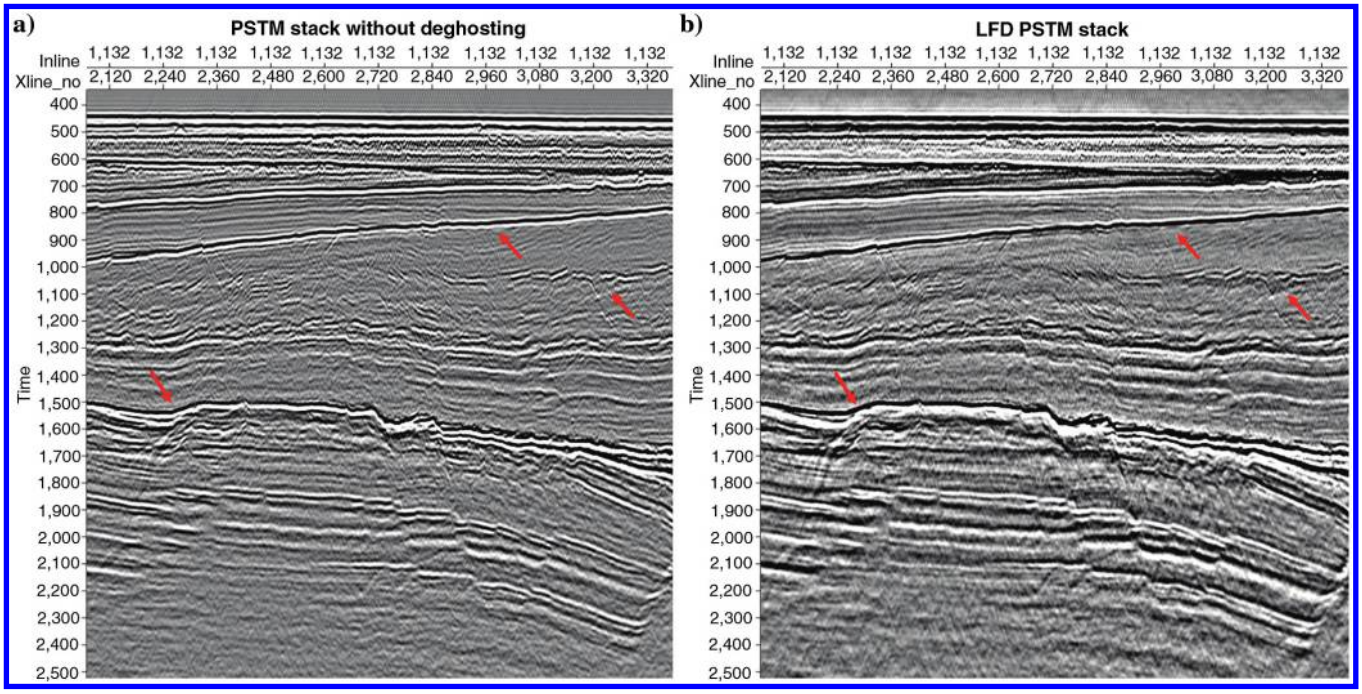

Figure 13. Field-data example from the Troll field. The prestack time-migrated results comparison (a) before and (b) after low-frequency deghosting on the receiver side (plus a dip filter). The red arrows point to examples of improved low-frequency content and prominent waveform correction effects after low-frequency deghosting.

prominent waveform correction effects after deghosting, for example, the events pointed out by the red arrows. In Figure 14, the corresponding amplitude spectra comparison of the migrated data sets is presented showing the low-frequency enhancement effect of our deghosting.

DISCUSSION

There are several attactive attributes of the proposed low-frequency deghosting method. It is a short operator that can be applied to conventional towed streamer data. In addition, a small slant or curvature in the steamer would not affect the effectiveness and localness of the method. The 3D exact deghosting operator is commonly expressed in the frequency-wavenumber domain or analogous domains because it is a function of the frequency and the take-off/incidence angle. The application of this operator requires 3D data sampled properly in both inline and crossline directions. This is necessary in order to perform the 3D Fourier transform to the 3D data to obtain ω, k_x, and k_y, i.e., the Fourier conjugate variables for t, x, and y. In practice, because the streamer data are poorly sampled in one of the horizontal directions (crossline), this in combination with new data-acquisition geometries with nonhorizontal streamers make the practical application of the exact deghosting operator a challenge and usually require several approximations and/or data conditioning and interpolation.

The low-frequency deghosting method presented here is an approximation to the exact 2D deghosting operator. It only requires a 1D Fourier transform along the time axis. The second-order spatial partial derivatives ∂_x^2 to the data in the operator's formulation provide the spatial filter aperture and partial compensation for the take-off/incidence angle information required in the exact operator. The application of this method uses actual 3D offsets, but operates cable by cable. As long as the coordinates of the sources/receivers are known, the low-frequency deghosting can be semilocally applied to 3D data, trace-by-trace, sequentially in the inline direction, using a few nearby traces to calculate the inline derivatives. The 3D application is within the assumptions of the 2D algorithm. In other words, the crossline direction is not considered due to its sparsity, and each cable is treated in a 2D sense. Of course, any method that is based on approximations has the common limitation of not being accurate everywhere. The effective range of this method, frequency-wise, decreases when the sources/receivers are towed deeper as the frequency of the first nonzero ghost notch becomes smaller and the operator loses accuracy at half of the value of that frequency. At each towing depth, take-off/incidence angle-wise, this method is equally effective, that is from 0° up to approximately 40°. In practice, as we did in the Troll data example, we propose to apply the low-frequency deghosting method only within its effective range, so that the ghost events in the low frequencies are removed, providing an overall attenuation of the adverse effects of ghosts in the measured streamer data.

During our numerous tests, we found that the boosted low frequency contains the useful signals and some low-frequency noise. In particular, what happens in the field data example above (the results shown on shot gathers, Figures 10–12) is not something particular to that data set: The boosted low-frequency noise is mostly outside of the main signal cone in the f-k domain. As such, the noise can be dealt with using a dip-filter (f-k filter) on shot gathers right after applying low-frequency deghosting. We also point out that the f-k transform of a shot gather acquired using a variable-depth streamer profile provides a distorted representation of the data actual wavenumbers and that may have an effect on the accuracy of the dip filtering. The effect should be small at low frequencies (less than 5%).

CONCLUSION

We have analyzed and tested an approximate deghosting method for towed streamer data that works well for low-frequency enhancement. This method is semilocal because it can be performed trace by trace using only a few neighboring traces for derivatives to the pressure data in the frequency-space (f-x) domain, as opposed to most of the conventional methods that require global transforms in the spatial axes. Its effective frequency range is between 0 Hz up to at least half of the first nonzero ghost notch. Because this method is accurate at low frequencies and can be effective in deghosting take-off/incidence angles up to approximately 40°, we believe it to be especially useful in deep-water scenarios and in enhancing deeper targets within a fixed offset range. We also expect this operator to be of practical advantage for fast-track processing, fast QC of other deghosting methods in the low-frequency range, and for inversion methods using the low frequencies in the data, such as full-waveform inversion.

In practice, this method can be targeted for conventional data with shallow tow. No changes in the algorithm are needed to process data acquired with gentle variations in the source depths, or receiver depths within a streamer. The method provides a fast (in terms of computational cost), stable (in terms of performance within its effective range), and local (in terms of spatial sampling and completeness of the data) low-frequency deghosting tool.

ACKNOWLEDGMENTS

We would like to thank L. Amundsen for valuable guidance and encouragement. We also thank our colleagues B. Wu and H. Yang for their insightful discussions and generous support. We thank the associate editor N. Gulunay and the reviewers S. Grion, A. B. Weglein, and R. D. Martinez for their constructive comments that helped to improve the paper. We thank Statoil and Troll license partners (Petoro, Shell, ConocoPhillips, and Total) for permission to publish this work.

REFERENCES

Amundsen, L., 1993, Wavenumber-based filtering of marine point-source data: Geophysics, **58**, 1335–1348, doi: 10.1190/1.1443516.

Amundsen, L., A. Reitan, A. B. Weglein, and B. Ursin, 2016, On seismic deghosting using Green's theorem: Geophysics, **81**, no. 4, V317–V325, doi: 10.1190/geo2014-0296.1.

Amundsen, L., and H. Zhou, 2013, Low-frequency seismic deghosting: Geophysics, **78**, no. 2, WA15–WA20, doi: 10.1190/geo2012-0276.1.

Andersson, F., A. C. Ramirez, T. Wiik, and V. V. Nikitin, 2016, Directional interpolation of multicomponent data: Geophysical Prospecting, doi: 10.1111/1365-2478.12478.

Carlson, D., 2007, Increased resolution of seismic data from a dual sensor streamer cable: 77th Annual International Meeting, SEG, Expanded Abstracts, 994–998.

Grion, S., R. Telling, and S. Holland, 2016, Phase-shift de-ghosting: 78th Annual International Conference and Exhibition, EAGE, Extended Abstracts, We-SRS3-09.

Hardwick, A., P. Charron, H. Masoomzadeh, A. Aiyepeku, P. Cox, and A. Laha, 2015, Accounting for sea surface variation in deghosting — A novel approach applied to a 3D dataset offshore west Africa: 85th Annual International Meeting, SEG, Expanded Abstracts, 4615–4619.

Klüver, T., and A. Day, 2011, Processing 3-D dual-sensor towed streamer data using local crossline slowness estimates: 81st Annual International Meeting, SEG, Expanded Abstracts, 3556–3560.

Masoomzadeh, H., and N. Woodburn, 2013, Broadband processing of conventional streamer data — Optimized de-ghosting in the tau-p domain: 75th Annual International Conference and Exhibition, EAGE, Extended Abstracts, Th-08-14.

Mayhan, J. D., and A. B. Weglein, 2013, First application of Green's theorem-derived source and receiver deghosting on deep-water Gulf of Mexico synthetic (SEAM) and field data: Geophysics, **78**, no. 2, WA77–WA89, doi: 10.1190/geo2012-0295.1.

Mellier, G., M. Maples, J. Hepp, S. LeBoeuf, and M. Lansley, 2014, A new multisensor solid streamer: 84th Annual International Meeting, SEG, Expanded Abstracts, 228–232.

Özbek, A., M. Vassallo, K. Özdemir, D.-J. van Manen, and K. Eggenberger, 2010, Crossline wavefield reconstruction from multicomponent streamer data: Part 2 — Joint interpolation and 3D un/down separation by generalized matching pursuit: Geophysics, **75**, no. 6, WB69–WB85, doi: 10.1190/1.3497316.

Poole, G., 2013, Pre-migration receiver de-ghosting and re-datuming for variable depth streamer data: 83rd Annual International Meeting, SEG, Expanded Abstracts, 4216–4220.

Robertsson, J. O. A., and L. Amundsen, 2014, Wave equation processing using finite-difference propagators, Part 2: Deghosting of marine hydrophone seismic data: Geophysics, **79**, no. 6, T301–T312, doi: 10.1190/geo2014-0152.1.

Robertsson, J. O. A., I. Moore, M. Vassallo, K. Özdemir, D.-J. van Manen, and A. Özbek, 2008, On the use of multicomponent streamer recordings for reconstruction of pressure wavefields in the crossline direction: Geophysics, **73**, no. 5, A45–A49, doi: 10.1190/1.2953338.

Soubaras, R., 2012, Pre-stack deghosting for variable-depth streamer data: 74th Annual International Conference and Exhibition, EAGE, Extended Abstracts, I019.

Tabti, D., A. Day, T. Schade, M. Lesnes, and T. Høy, 2009, Conventional versus dual-sensor streamer data de-ghosting: A case study from a Haltenbanken survey: First Break, **27**, 101–108.

Ten Kroode, F., S. Bergler, C. Corsten, J. W. De Maag, F. Strijbos, and H. Tijhof, 2013, Broadband seismic data — The importance of low frequencies: Geophysics, **78**, no. 2, WA3–WA14, doi: 10.1190/geo2012-0294.1.

van Manen, D.-J., P. Christie, K. Eggenberger, M. Vassallo, A. Ozbek, S. Zeroug, E. Kragh, and T. Curtis, 2012, Increasing spatial and temporal bandwidth with multi-component streamer data: 74th Annual International Conference and Exhibition, EAGE, Extended Abstracts, 1524–1532.

Wang, Y., A. C. Ramirez, and S. Nag, 2016, A 3D deghosting solution for pressure-only measurements of conventional towed streamer data: 78th Annual International Conference and Exhibition, EAGE, Extended Abstracts, We-SRS3-15.

Wang, Y., H. Yang, A. Osen, and L. Amundsen, 2013, A new local method for seismic deghosting of towed streamer data: 75th Annual International Conference and Exhibition, EAGE, Extended Abstracts, We-P08-09.

Weglein, A. B., S. A. Shaw, K. H. Matson, J. L. Sheiman, R. H. Stolt, T. H. Tan, A. Osen, G. P. Correa, K. A. Innanen, Z. Guo, and J. Zhang, 2002, New approaches to deghosting towed streamer and ocean-bottom pressure measurements: 72nd Annual International Meeting, SEG, Expanded Abstracts, 1016–1019.

Yarman, E., and A. C. Ramirez, 2013, Directional wavefield decomposition: Geophysics, **78**, no. 2, WA71–WA76, doi: 10.1190/geo2012-0324.1.

Zhang, J., and A. B. Weglein, 2005, Extinction theorem deghosting method using towed streamer pressure data: Analysis of the receiver array effect on deghosting and subsequent free surface multiple removal: 75th Annual International Meeting, SEG, Expanded Abstracts, 2095–2098.